Unrestrained growth of correctly oriented microtubules instructs axonal microtubule orientation

Maximilian AH Jakobs[1,*], Assaf Zemel[2], Kristian Franze[1,3,4,*]

[1] Department of Physiology, Development and Neuroscience, University of Cambridge, Downing Street, Cambridge, CB2 3DY, UK.

[2] Institute of Biomedical and Oral Research, and the Fritz Haber Center for Molecular Dynamics, Hebrew University of Jerusalem, 91120 Jerusalem, Israel.

[3] Institute of Medical Physics, Friedrich-Alexander University Erlangen-Nuremberg, Henkestr. 91, 91052 Erlangen, Germany.

[4] Max-Planck-Zentrum für Physik und Medizin, 91054 Erlangen, Germany

* Correspondence: mj455@cam.ac.uk and kf284@cam.ac.uk

Summary

In many eukaryotic cells, directed molecular transport occurs along microtubules. Within neuronal axons, transport over vast distances particularly relies on uniformly oriented microtubules, whose +-ends point towards the distal axon tip (+end out). However, axonal microtubules initially have mixed orientations, and how they orient during development is not yet fully understood. Using live imaging of primary *Drosophila melanogaster* neurons and physical modelling, we found that +end out microtubules are less likely to undergo catastrophe near the advancing axon tip, leading to their persistent long-term growth. In contrast, oppositely oriented microtubules remain short. Using chemical and physical perturbations of microtubule growth and genetic perturbations of the anti -catastrophe factor p150, which was enriched in the distal axon tip, we confirmed that the enhanced growth of +end out microtubules is critical for achieving uniform microtubule orientation. Computer simulations of axon development mimicking the enhanced +end out microtubule growth identified here along with previously proposed mechanisms correctly predicted the long-term evolution of axonal microtubule orientation as found in our experiments, highlighting the importance of the reduced catastrophe rate of +end out microtubules near the advancing axon tip in establishing uniform microtubule polarity. Our study thus leads to a holistic explanation of how axonal microtubules orient uniformly, a prerequisite for efficient long-range transport essential for neuronal functioning.

33 **Introduction**

34 Symmetry breaking is critical for many biological systems. An organism starts of as a single round
35 cell that divides and differentiates into many cells, tissues and organ systems. The neuron, with
36 its branched dendrites and sometimes exceedingly long axon, is one of the least symmetric cells
37 found in animals. Axons connect neurons with distant targets and thus enable long-distance
38 signal transmission throughout the body at high speed.

39 The enormous length of axons, which can extend over several meters in some vertebrate species,
40 poses substantial logistical challenges. RNA, proteins, and organelles originating in the cell body
41 need to be actively transported down the axon. Transport occurs along MTs, which are long,
42 polarized polymers that undergo stochastic cycles of growth and shrinkage (**FIGURE 1A)**. Motor
43 proteins transport cargo either towards a MT's dynamic (i.e., growing or shrinking) +end, or the
44 stabilized -end.

45 In immature axons, MT orientation is mixed, with 50-80% of all MTs pointing with their +end out
46 (del Castillo et al., 2015; Yau et al., 2016a). During early neuronal development, the fraction of
47 +end out axonal MTs increases (del Castillo et al., 2015; Yau et al., 2016a). In mature axons, ~95%
48 of all MTs point in the same direction (+end out) (Baas et al., 1989; Heidemann et al., 1981),
49 enabling polarized transport (Millecamps and Julien, 2013). Deficits in polarized transport have
50 been associated with human neurodegenerative diseases, such as Alzheimer's and Parkinson's
51 disease (Millecamps and Julien, 2013). Despite the importance of polarized transport in neuronal
52 axons, the mechanisms that establish and maintain MT orientation are still not fully understood
53 (Baas and Lin, 2011; Conde and Cáceres, 2009; Kapitein and Hoogenraad, 2011).

54 MTs in post-mitotic neurons are not attached to the centrosome (Kuijpers and Hoogenraad,
55 2011). Nucleation of new MTs occurs from MT organising centres (MTOCs) such as somatic Golgi
56 (Mukherjee et al., 2011) through elongation of severed pieces (Yu et al., 2008) or *de novo*
57 polymerization alongside existing MTs (Nguyen et al., 2014; Sánchez-Huertas et al., 2016). These
58 newly formed MTs often orient in the same direction as existing ones, enforcing any pre-existing
59 orientation bias (Mattie et al., 2010; Mukherjee et al., 2020). Pre-existing biases are furthermore
60 enhanced by selective stabilisation of MTs through TRIM46-mediated parallel bundling (van
61 Beuningen et al., 2015). However, without pre-existing biases these mechanisms by themselves
62 cannot explain the robust +end out orientation of MTs in mature axons.

63 Furthermore, in axons, short MTs pointing with their -end away from the cell body can be
64 transported towards the cell body (i.e., away from the tip) by cytoplasmic dynein (del Castillo et
65 al., 2015; Rao et al., 2017), thus potentially clearing the axon of -end out MTs. To test whether
66 this mechanism is sufficient to establish uniform microtubule orientation in axons, we previously
67 designed computer simulations of dynein-mediated MT sliding in neurons. However, while MTs
68 in the distal axon were oriented mostly with their +end away from the cell body {Jakobs:2015hk,
69 Jakobs:2020jg}, our simulations failed to explain the longer-term +end out orientation of MTs in
70 the proximal axon and the gradual establishment of a uniform +end out MT orientation
71 throughout the axon seen in experiments ({Yau:2016jv}). Thus, our simulations suggested that
72 additional mechanisms are needed to establish the uniform +end out orientation of MTs in
73 neuronal axons.

74 Here, we investigated MT growth behaviours along *Drosophila melanogaster* axons and
75 discovered a growth bias of +end out MTs near the advancing axon tip, which depended on the
76 presence of MT anti-catastrophe protein gradients in the distal axon. A stochastic model of MT
77 dynamics suggested that this growth bias leads to unbounded growth of these MTs, while -end
78 out MTs remain short. Experiments and computer simulations confirmed that the observed
79 selective growth bias is critical for uniform axonal MT orientation, leading to a model integrating
80 known mechanisms with the decreased +end out MT catastrophe rate discovered here to explain
81 how uniform MT orientation is achieved in developing neuronal axons.

82

83 **Results**

84 ***Correctly oriented MTs add more length per growth cycle***

85 To investigate how MT orientation in neuronal axons becomes biased, we first cultured acutely
86 dissociated neurons from the *Drosophila melanogaster* larval CNS (Egger et al., 2013) and
87 quantified MT growth in axons. We used *Drosophila* lines expressing the fusion protein EB1-GFP,
88 which labels growing MT +ends with bright 'comets' (**FIGURE 1A-C**) (Sanchez-Soriano et al., 2010;
89 Stepanova et al., 2003). The distance over which a comet moves in the axon is equal to the overall
90 length d_g that is added to a MT between the start of its growth cycle and the catastrophe leading
91 to MT shrinkage (**FIGURE 1A)**. The direction of growth reveals whether a MT is oriented with its
92 +end away from (+end out) or towards (-end out) the cell body. Time-lapse movies of EB1-GFP

comets were converted into kymographs and analysed using *KymoButler* (Jakobs et al., 2019) (**FIGURE 1D-F**).

The fraction of +end out MTs increased over time and with increasing axonal length (**FIGURE 1G-H**), confirming that MT orientation increases during development (del Castillo et al., 2015; Yau et al., 2016a). Most MT growth events (~66%) were found within the first 20 µm from the advancing axon tip (**FIGURE 1A, J**). MT growth lengths per cycle, d_g, were significantly higher near the axon tip compared to further away from it (**FIGURE 1K**). Furthermore, +end out MTs added significantly more length per growth cycle than -end out MTs, with the highest difference between +end out and -end out MTs (~0.5 µm/cycle) found within the first 10 µm from the axon tip (d_g (+end out)= 2.11 [2.04, 2.16] µm / cycle & d_g (-end out)= 1.39 [1.27, 1.50] µm, bootstrapped median [95% confidence interval]) (**FIGURE 1L**).

Increases in MT growth lengths during a polymerisation cycle $d_g = v_g/f_g$ could either arise from an increased polymerization velocity v_g or a decreased catastrophe frequency f_g (or both). In *drosophila* neurons, MT growth velocities v_g were similar in all MTs irrespective of their orientation and position within the axon (~5 µm / min; ERROR! REFERENCE SOURCE NOT FOUND.**C**). Additionally, EB1-GFP, which affects microtubule polymerisation velocities, was not enriched at the axon tip (ERROR! REFERENCE SOURCE NOT FOUND.**E**), and EB1-GFP comet lengths, which have previously been linked to microtubule polymerisation speeds (Roostalu et al., 2020), did not show significant variations along the axon (ERROR! REFERENCE SOURCE NOT FOUND.**F**). However, catastrophe rates $f_g = 1/t_g$ were significantly lower (and thus polymerization times t_g significantly longer) in +end out MTs near the axon tip ($f_{g+} \sim 4 * 10^{-2} sec^{-1}$ *vs.* $f_{g-} \sim 6 *$

$10^{-2} sec^{-1}$; ERROR! REFERENCE SOURCE NOT FOUND.**B**), suggesting that these MTs grew longer because of a decrease in their catastrophe frequencies.

Overall, the orientation of MTs that added more length per growth cycle (i.e., +end out MTs) becomes the dominant MT orientation in developing axons, indicating a possible link between increased +end out MT growth and the fraction of +end out MTs in axons.

Enhanced growth of +end out MTs leads to unbounded growth

On long time scales, differences in MT growth length per growth cycle accumulate and thus affect the average MT length l_{MT}. To estimate whether the rather small differences in d_g of ~0.5 µm/cycle might lead to biologically meaningful differences in the average expected MT lengths between +end out and -end out oriented MTs, we used a 2-state Master equation model of MT growth and shrinkage (see (Dogterom and Leibler, 1993) & supplemental methods for details). The model distinguishes two regimes (**FIGURE 2A**):

$$l_{MT} = \begin{cases} d_g d_s/(d_s - d_g) & d_s > d_g \quad \text{('bounded' growth)} \\ \infty & d_s \leq d_g \quad \text{('unbounded' growth)} \end{cases} \tag{1}$$

where d_s = lost length per shrinkage cycle.

When $d_s \leq d_g$, the average length added to the MT exceeds the average shrinkage length per cycle so that an MT will exhibit net growth and elongate if physically possible in its confined environment (called 'unbounded' growth). For $d_s > d_g$, however, growth is 'bounded', and average MT lengths follow an exponential distribution with a mean of $d_s d_g/(d_s - d_g)$. In practice,

132 this means that MTs with $d_g \geq d_s$ would grow until encountering a physical barrier (for example
133 the distal end of the axon tip), while MTs with $d_s > d_g$ remain finite (for example, approximately
134 2 µm with d_s = 2 µm and d_g = 1.5 µm).

135 We determined the MT shrinkage per cycle d_s by co-expressing a Jupiter-mCherry fusion protein
136 (a tubulin marker) together with EB1-GFP in *D. melanogaster* axons. MTs stopped growing when
137 the GFP signal disappeared from their +end, indicating a catastrophe or pause event. Subsequent
138 MT shrinkage was visualized by simultaneously imaging tubulin (Jupiter-mCherry) and quantified
139 by tracing tubulin edges resulting from the shrinkage in the dual colour kymographs (**FIGURE 2B-**
140 **D**). Axonal MT shrinkage lengths were d_s = 2.03 [1.80, 2.26] µm / cycle (bootstrapped median
141 [95% confidence interval], **FIGURE 2E**).

142 With this value for d_s, our model predicted the divergence of l_{MT} at d_g = 2.03 µm, at the lower end
143 of the measured 95% confidence interval for the median d_g = [2.04, 2.16] µm / cycle of +end out
144 MTs near the axon tip but well above the 95% confidence interval for the median d_g = [1.39, 1.48]
145 µm / cycle of all other MTs (**FIGURE 2F).** The measured values of d_g *and* d_s hence suggested that
146 +end out-oriented MTs exhibit mostly unbounded growth within 10 µm from the axon tip while
147 -end out MTs within that range and any MT further away from the tip do not (**FIGURE 2F)**. The
148 decreased catastrophe frequency of +end out MTs near the axon tip (ERROR! REFERENCE SOURCE
149 NOT FOUND.**A-C**) implied a higher chance of survival for +end out MTs while leaving -end out MTs
150 labile, thereby establishing a bias for +end out microtubule orientation.

151

152 ***Enhanced growth of +end out MTs is required for uniform +end out MT orientation***

153 To test if enhanced MT growth is indeed involved in biasing MT orientation, we first chemically
154 decreased MT growth using Nocodazole, a drug that disrupts MT polymerization. Nocodazole
155 treatment led to decreased MT growth velocities v_g (**Error! Reference source not found.**).
156 Alternatively, we also physically decreased MT growth by increasing the osmolarity of the cell
157 culture medium through addition of NaCl (BRAY et al., 1991; Molines et al., 2020). Here, MT
158 catastrophe rates f_g were significantly increased (**Error! Reference source not found.**).

159 Both treatments led to significantly decreased +end out MT growth $d_g = v_g/f_g$ at the axon tip
160 (< 10 µm), with d_g < 1.71 µm / cycle < d_s (upper 95% confidence bound of median) (**FIGURE 3A-E**).
161 Our model predicted that this change in d_g should lead to a switch from previously unbounded
162 to bounded growth of +end out MTs near the axon tip (**FIGURE 3D**), thus reducing the bias towards
163 +end out MTs and decreasing MT orientation. In agreement, MTs within treated axons were
164 overall significantly less uniformly oriented (**FIGURE 3D-E**), confirming an important role of the
165 enhanced growth lengths per cycle of +end out MTs in establishing axonal MT orientation.

166

167 ***p150 protein gradient in axon tips promotes +end out MT stabilisation***

168 However, why do +end out MTs grow longer in the vicinity of the axon tip? Local gradients of MT
169 growth-promoting factors could lead to an increase in +end MT growth in that region. Axon tips
170 contain a multitude of different proteins and are highly compartmentalised (Lowery and Van
171 Vactor, 2009). Locally enriched MT growth-promoting factors (of which there are many in the

172 axon tip (Voelzmann et al., 2016)), include MT stabilizing proteins, such as p150 (Lazarus et al.,
173 2013; Moughamian and Holzbaur, 2012), CRMP-2 (Fukata et al., 2002; Inagaki et al., 2001), and
174 TRIM46 (Rao et al., 2017; van Beuningen et al., 2015), as well as free tubulin and others (Eng et
175 al., 1999).

176 The MT stabilizing protein p150, for example, affects MT catastrophe rates f_g and nucleation
177 rates but not growth velocities v_g (Lazarus et al., 2013). As we observed decreased MT
178 catastrophe rates but constant growth velocities of +end out MTs towards axon tips (**Error!**
179 **Reference source not found.B, C**), we hypothesised that p150 is one of the key proteins involved.
180 *Drosophila* has a p150 homologue which, similar as in murine neurons (Moughamian and
181 Holzbaur, 2012), we found to be enriched in axonal but not in dendritic tips (**Figure 4A, C** and
182 **Error! Reference source not found.**). Accordingly, +end out MT growth lengths per cycle d_g and
183 catastrophe rates f_g were significantly higher in axons than in dendritic processes (ERROR!
184 REFERENCE SOURCE NOT FOUND.**E,G**), where d_g = 1.42 [1.37, 1.39] µm / cycle remained smaller than
185 d_s = 2.03 [1.80, 2.26] µm / cycle. In agreement with our model, which predicted unbounded
186 growth of +end out MTs in axons but bounded growth in dendritic processes (**Figure 2**), dendritic
187 processes exhibited mixed (50% +end out) MT orientations (ERROR! REFERENCE SOURCE NOT
188 FOUND.**D**), corroborating a link between MT stabilizing protein gradients in the tip of axons,
189 reduced MT catastrophe rates, unbounded growth, and overall MT orientation.

190 We next tested whether the observed p150 gradient is strong enough to lead to different MT
191 growth lengths (via modulation of catastrophe rates, $d_g \sim 1/f_g$) for +end out and -end out MTs
192 within 10 µm from the axon tip, the region where we observed the largest differences in f_g

193 (**Error! Reference source not found.C**). We assumed that MT growth lengths per cycle at a
194 distance *x* from the axon tip can be described by a power law function $d_g(x) = A*p150(x)^{\alpha}$ of the
195 p150 fluorescence intensity profile. A simultaneous fit to both +end out and -end out MTs
196 demonstrated that the observed gradient is, in theory, indeed strong enough to cause different
197 growth behaviours for +end out and -end out MTs in axonal tips (ERROR! REFERENCE SOURCE NOT
198 FOUND.).

199 To test this prediction further, we assessed MT dynamics in *wild-type*, *p150-RNAi* expressing
200 neurons, and in neurons from $p150^1$/+ mutant flies (**Figure 4**). $p150^1$ (also known as Gl^1) mutants
201 express a truncated p150-RNA transcript, which results in a dominant negative phenotype
202 (Plough and Ives, 1935). Expressing *p150-RNAi* led to decreased p150 protein in axons (**Figure**
203 **4A-C)**. Both the expression of *p150-RNAi* and of dominant negative $p150^1$/+ led to a significant
204 increase in +end out MT catastrophe rates (**Error! Reference source not found.**) and thereby to
205 a decrease (14%-20%) in +end out MT growth within 10 µm from the axon tip (**Figure 4G**). In
206 agreement with our model, the overall axonal MT orientation was significantly decreased in both
207 *p150-RNAi* and $p150^1$/+ axons compared to controls (**Figure 4H**).

208 p150 is known to interact with dynein (Karki and Holzbaur, 1995). Expressing an RNAi against
209 dynein heavy chain also led to decreased +end out MT growth at the axon tip (25%) and
210 decreased MT organisation, reproducing the results of p150 removal (ERROR! REFERENCE SOURCE
211 NOT FOUND.). Together, these data indicated that MT stabilising or growth-promoting protein
212 gradients at the axon tip do indeed have an important role in regulating the overall orientation
213 of the axonal MT network.

214

215 ***Kinesin 1 is required to establish p150 gradient***

216 Previous work showed that p150 accumulation at axon tips depends on the activity of the MT-
217 specific molecular motor protein kinesin 1 (Moughamian and Holzbaur, 2012; Twelvetrees et al.,
218 2016), which preferentially enters axons over dendrites (Tas et al., 2017). Accordingly, disruption
219 of kinesin 1 function with an RNAi treatment led to a 25% decrease in p150 fluorescence within
220 10 µm from the axon tip (ERROR! REFERENCE SOURCE NOT FOUND.**A-D**). Again, the absence of a p150
221 gradient in these neurons led to a significant increase in MT catastrophe rates and decreased
222 +end out MT growth near the axon tip, and hence to an overall decrease in axonal MT orientation
223 (ERROR! REFERENCE SOURCE NOT FOUND.**E-I**), suggesting that gradients of MT-stabilising proteins at
224 the tips of developing axons are critical for biasing axonal MT orientations.

225

226 ***Uniform axonal MT orientation is established through a combination of MT sliding, templating,***
227 ***and unbounded growth***

228 Our experiments suggested that a gradient of a MT growth-promoting factor localised at the axon
229 tip is required for establishing uniform +end out MT orientation in axons. To investigate the
230 significance of the locally biased microtubule growth in more detailed, we modelled the evolution
231 of overall microtubule polarity along the axon using computer simulations. We extended our
232 previously described simulations (Jakobs et al., 2020) to include two additional effects on axonal
233 MTs: (1) enhanced stabilization of MTs at axon tips as found in this study, and (2) a local biasing

234 of MT nucleation (MT templating) that could originate from augmin (Nguyen et al., 2014;
235 Sánchez-Huertas et al., 2016) or TRIM46 (van Beuningen et al., 2015).

236 The simulation is detailed in the methods section and a schematic can be found in **FIGURE 5A**.
237 Briefly, a cylindrical bundle of MTs is generated, and dynein motors are assumed to cross-link
238 adjacent MTs. The orientation of each MT is randomly chosen. Force-velocity relationships are
239 used to predict the exerted sliding velocities of the MTs, which are then used to calculate new
240 MT positions iteratively. MTs were confined in the axon with a solid boundary at the axon tip and
241 a semi-permeable boundary at the cell body. New MTs were added randomly along the bundle
242 axis at a determined frequency. To mimic the effect of a concentration gradient of a growth-
243 promoting protein (such as p150) at the axon tip, we assumed that the frequency of newly added
244 MTs is sampled from an exponential distribution that peaks at the axon tip. To account for augmin
245 or TRIM46-induced local biases of MT nucleation, we assumed that the orientation of an added
246 MT is dictated by the mean MT-orientation in the region to which it is added.

247 Simulations incorporating dynein-induced MT sliding but lacking mechanisms (1) and (2)
248 mentioned above resulted in steadily growing axons whose MT orientation profile was graded
249 along their length, being enriched with +end out MTs at the distal end and with –end out MTs at
250 the proximal (cell body) end (**FIGURE 5A,B, E AND** ERROR! REFERENCE SOURCE NOT FOUND.). The
251 proximal domain of –end out MTs grew in proportion to the axon length, as –end out MTs from
252 across the growing axon continually accumulated in that region despite their withdrawal into the
253 cell body by dynein motors. Those simulations thus failed to reproduce the experimental

254 observation of an enrichment of the proximal axon with +end out MTs over time, which
255 eventually leads to uniformly oriented axonal MTs (Yau et al., 2016b) (**FIGURE 5D**).

256 Similarly, the increased growth of +end out microtubules or templating alone, or any combination
257 of two out of these three mechanisms, were also insufficient for establishing high fractions of
258 +end out MTs at the proximal axon as observed experimentally (ERROR! REFERENCE SOURCE NOT
259 FOUND.).

260 However, when we integrated sliding, templating, and biased MT growth at the axon tip in the
261 simulation (assuming that the likelihood of exhibiting unbounded growth corresponds to a
262 successful nucleation event), MTs gradually oriented uniformly +end out across the entire length
263 of the axon, recapitulating our experimental results (**FIGURE 5C, D, F AND** ERROR! REFERENCE SOURCE
264 NOT FOUND.). Thus, our data suggest that multiple mechanisms – including biased growth of +end
265 out MTs near the axon tip identified in this study – need to work in unison to establish and
266 maintain uniform axonal microtubule orientation.

267

268 **Discussion**

269 We here found that MT growth is an important factor in the regulation of overall MT organisation
270 in the axon. Our experiments and modelling suggest that an enrichment of MT stabilising /
271 growth-promoting proteins at the advancing axon tip leads to a transition of MT growth from a
272 bounded to an unbounded state for +end out MTs. This growth transition is important for
273 establishing uniform +end out MT orientation from the cell body to the axon tip as found in

274 mature axons. While previous studies suggested that MT dynamics are temporally and spatially
275 constant during early axon formation (Seetapun and Odde, 2010), our results suggest that, at
276 later stages of axon maturation, MT dynamics are heterogeneous (**FIGURE 1**).

277 Our chemical and physical perturbations of MT growth affected different aspects of MT dynamics.
278 Nocodazole treatment decreased MT growth velocities while not affecting catastrophe
279 frequencies; hyperosmotic solutions increased MT catastrophe frequencies but did not alter
280 growth velocities (**Error! Reference source not found.**). The effect of the hyperosmotic solution
281 might potentially arise from a decrease in the available space in the distal axon for MTs to
282 polymerize into (Dogterom and Yurke, 1997; Franze, 2020). However, NaCl can be toxic for
283 neurons, so that the effect on MT growth could also be due to a general stress response (Morland
284 et al., 2016). Either way, both treatments led to a decrease of the microtubule length added
285 during each growth cycle, d_g, so that $d_g < d_s$, switching +end out MT dynamics from unbounded
286 to bounded growth, thus leading to a loss of uniform MT polarisation along the axon (**Figure 3**).

287 The axon tip is highly enriched with growth promoting factors such as p150 (Lazarus et al., 2013;
288 Moughamian and Holzbaur, 2012), CRMP-2 (Fukata et al., 2002; Inagaki et al., 2001), TRIM46
289 (Rao et al., 2017; van Beuningen et al., 2015) and EB1 (Ma et al., 2004; Morrison et al., 2002). The
290 MT stabilising protein p150, which we investigated here as an example, was concentrated at axon
291 tips but was not enriched at dendritic tips (**Error! Reference source not found.).** Enhanced
292 stabilisation of +end out MTs, leading to reduced catastrophe rates and thus unbounded growth
293 essential for establishing uniform MT orientation, was only observed near axonal but not near
294 dendritic tips (ERROR! REFERENCE SOURCE NOT FOUND.), confirming that differences in the

295 localization of MT growth-promoting proteins correlate with differences in MT growth.
296 Perturbations of p150 led to increased catastrophe rates and decreased +end out MT growth in
297 the axon tip, and thus to decreased overall MT order in the axon (**FIGURE 3**).

298 While p150 is mainly known for of its role in the dynactin complex, which is an important cargo
299 adapter protein complex for the molecular motor protein dynein (Gill et al., 1991), it also acts as
300 a dynein-independent MT anti-catastrophe factor (Lazarus et al., 2013). Since p150 and dynein
301 are functionally related, it is difficult to separate their individual contributions to stabilising +end
302 out MT growth in the axon tip and cell body-directed sliding of -end out MTs along the axon.
303 However, it remains unclear whether p150 is required for dynein-mediated MT sliding (Ahmad
304 et al., 1998; Waterman-Storer et al., 1997), and the *Drosophila melanogaster* oocyte also
305 contains a biased MT cytoskeleton whose orientation is, presumably, maintained by p150
306 (Nieuwburg et al., 2017). Hence, while p150 is unlikely to induce unbounded MT growth alone, it
307 emerges as a key contributor to the establishment of MT orientation.

308 In addition to its contribution to setting up the p150 gradient in axon tips (ERROR! REFERENCE
309 SOURCE NOT FOUND.)**,** kinesin 1 is also thought to slide MTs with their -end leading (del Castillo et
310 al., 2015) and to be involved in dynein function (Pilling et al., 2006; Rao et al., 2017). Kinesin
311 knockdown could thus not only prevent the accumulation of MT growth-promoting factors at the
312 axon tip but also decrease kinesin 1-mediated -end out MTs sliding into the distal axon (thereby
313 increasing the fraction of +end out MTs) and/or prevent retrograde dynein-mediated sliding of -
314 end out MTs (decreasing the fraction of +end out MTs). We observed that disruption of kinesin
315 1 function led to a decrease in the fraction of +end out MTs in the axon (ERROR! REFERENCE SOURCE

316 NOT FOUND.), suggesting that kinesin 1 does not contribute to the overall MT orientation via direct
317 sliding but that it rather affects MT orientation mainly via localising MT growth or nucleation-
318 promoting proteins to axonal tips and/or via interactions with dynein-mediated sliding.

319 Finally, both kinesin 1 and p150/dynactin perturbations could potentially also affect MTOC
320 localization in neurons. p150 was enriched at the tips of axonal but not of dendritic processes
321 (ERROR! REFERENCE SOURCE NOT FOUND.). In *C. elegans* neurons, MTOCs may be located to the tips
322 of dendritic processes (Liang et al., 2020). Removal of dynactin, which initiates cell body-directed
323 transport from axonal tips (Moughamian and Holzbaur, 2012), could lead to an increased number
324 of MTOCs also at axon tips, thereby promoting growth and nucleation of MTs. However, our
325 results showed a decrease in MT growth dynamics at axon tips after dynactin removal (**FIGURE 3**),
326 indicating that the observed decrease in MT orientation was mostly due to decreased rather than
327 promoted growth of axonal MTs in the axon tip.

328 We propose the following model explaining the spontaneous establishment of MT orientation in
329 developing axons. Growth-promoting proteins accumulate at the axon tip due to MT +end-
330 directed transport by kinesin motors (ERROR! REFERENCE SOURCE NOT FOUND.). The resulting protein
331 gradient leads to a local bias in MT growth (**FIGURE 1**, **FIGURE 3**), rendering +end out MT growth
332 into the axon tip unbounded (**FIGURE 2**). In theory, a finite pool of tubulin at axon tips would
333 further contribute to this bias in +end out MT growth by diminishing the amount of free tubulin
334 available for MTs that polymerise towards the cell body. In contrast, short -end out MTs are more
335 prone to depolymerization and/or transport away from the tip by dynein-mediated cell body-
336 directed sliding (del Castillo et al., 2015; Rao et al., 2017), thus contributing to the orientation

337 bias of MTs in the axon. The orientation bias is further enhanced by augmin-mediated templating
338 or TRIM46-mediated parallel bundling of newly formed MTs to establish and maintain a fully
339 organized MT cytoskeleton (see **FIGURE 5E** for a schematic summary). Together with cell process
340 length-dependent MT accumulation (Seetapun and Odde, 2010), these mechanisms cooperate
341 to build the polarized MT network that enables efficient long-range transport in neuronal axons.
342 Future work will reveal whether other cellular systems use similar mechanisms to organize their
343 cytoskeleton.

344 **Materials and Methods**

345 ***Key Resource Table***

Reagent or Resource	Source	Identifier
Experimental Models: Organisms/Strains		
D. melanogaster: EB1-GFP	(Bulgakova et al., 2012)	N/A
D. melanogaster: ubi EB1-GFP	(Shimada et al., 2006)	N/A
D. melanogaster: Jupiter-mcherry	(Bergstralh et al., 2015)	N/A
D. melanogaster: p150^{1}	Bloomington	RRID:BDSC_504
D. melanogaster: p150-RNAi	Bloomington	RRID:BDSC_3785
D. melanogaster: khc-RNAi	Bloomington	RRID:BDSC_35770
D. melanogaster: elav-gal4	Bloomington	RRID:BDSC_458
Antibodies		

Rb anti-p150	(Nieuwburg et al., 2017)	N/A
Ms anti-alpha-tubulin	Abcam	Cat#: ab7291 RRID:AB_2241126
Celltracker™	Invitrogen	Cat#: C2925
CF633 anti-Rb	Cambridge Bioscience	Cat#: BT20125
AF405 anti-Ms	Thermo Fisher	Cat#: ab175658 RRID:AB_2687445

Software and Algorithms

MATLAB	Mathworks	RRID:SCR_001622
Mathematica	Wolfram	RRID:SCR_014448
KymoButler	(Jakobs et al., 2019)	https://gitlab.com/ deepmirror/kymobutler
ImageJ	(Schindelin et al., 2012)	RRID:SCR_003070
Neurite Tracer	(Pool et al., 2008)	RRID:SCR_016566

346

347 ***Fly stocks***

348 MT +end dynamics were visualized with a transgenic fly line expressing EB1-GFP heterozygously
349 under its endogenous promoter (*wh;+;eb1-gfp/tm6b,* gift from the Brown laboratory in
350 Cambridge) (Bulgakova et al., 2013) or a fly expressing EB1-GFP under a *ubiquitin* promotor
351 (*ubi:eb1-gfp;+;+,* gift from the St. Johnston laboratory in Cambridge) (Shimada et al., 2006).
352 Whole MTs were labelled with Jupiter-mcherry (*wh;if/cyo;Jupiter-mcherry*, gift from the St.
353 Johnston laboratory in Cambridge) (Bergstralh et al., 2015). Other stocks used: *p150*^{1}
354 (Bloomington # 504)*, uas:p150-RNAi* (Vienna Drosophila Stock Center # 3785), *uas:khc-RNAi*
355 (Bloomington # 35770), *khc27* (Bloomington # 67409), khc17 (gift from the St. Johnston
356 laboratory in Cambridge). *uas* constructs were driven by *elav-gal4* (Bloom# 458, *elav* is a neuron
357 specific promotor that ensures the construct is only expressed in the CNS (Yannoni and White,
358 1997)) and transgenic lines were generated through standard balancer crossing procedures.

359 ***Primary cell culture***

360 3rd instar larvae were picked 5-8 days post fertilisation, and their CNS dissected similarly to
361 (Egger et al., 2013; Sanchez-Soriano et al., 2010). As described in (Egger et al., 2013) the resulting
362 primary culture comprised a mixture of terminally differentiated larvae neurons such as
363 peripheral neurons alongside precursors cells and immature neurons of the adult fly brain.
364 Thereby, the larval CNS lends itself to the study of a heterogenous population of neurons. The
365 CNS tissue was homogenized and dissociated in 100 µl of Dispersion medium (Hank's Balanced
366 Salt Solution (1xHBSS, Life Technologies, 14170088) supplemented with Phenylthiourea (Sigma-
367 Aldrich P7629, 0.05mg/ml), Dispase (Roche 049404942078001, 4mg/ml), and Collagenase

368 (Worthington Biochem. LS004214, 1mg/ml)) for 5 minutes at 37°C. The media was topped up
369 with 200 µl of Cell Culture Medium (Schneider's Medium, Thermo Fisher 21720024)
370 supplemented with insulin (2 µg/ml Sigma I0516) and fetal bovine serum (1:5 Thermo Fisher
371 Scientific A3160801)) and cells were spun down for 6 min at 650 rcf. The pellet was resuspended
372 in Cell Culture Medium at 5 brains/120 µl. Cells were grown at 26°C for 1.5 hours in a droplet of
373 30 µl Cell Culture Medium in a glass bottom dish between a Concanavalin A-coated glass slide
374 and an uncoated glass slide on top. Initially the cells were cultured with the coated coverslip
375 facing down. After 1.5 hours the chambers were flipped so that cells that did not attach floated
376 off to the opposite (uncoated) side. Culture times were: 4-26 hours (for measuring MT
377 orientation profiles in short and long axons), 22-26 hours (for measuring MT dynamics, both
378 Patronin-YFP and EB1-GFP), and 22-48 hours (for measuring MT dynamics in dendritic processes).

379 To measure the effect Nocodazole has on MT orientation in axons, the medium was
380 supplemented with 5uM of Nocodazole (Dissolved in DMSO, Sigma-Aldrich M1404-2MG)
381 approximately 12h post-plating and 12h before measuring MT dynamics. The control cells were
382 treated with 0.025% DMSO in culture medium. Treatment and corresponding controls were
383 always run in parallel, and when possible, from the same fly stock. *Uas* driven overexpression
384 was controlled with a fly expressing both *elav::gal4* and *eb1-gfp* to control for the expression of
385 gal4 protein.

386 To measure the effects of osmolarity changes in the surrounding medium we increased the
387 osmolarity of the culture medium by approximately 100 mOsm (from ~360 mOsm to ~460mOsm,
388 see also https://www.sigmaaldrich.com/GB/en/product/sigma/s9895) by adding 4mg of NaCl to

389 1ml Culture medium. Cells were first cultured in normal media for 1.5h. Subsequently, the media
390 was removed and replaced with either fresh media (control) or media supplemented with 4g
391 NaCl. Cells were again imaged after 22-26h post plating.

392 ***Live imaging of MTs***

393 All live imaging movies were acquired on a Leica DMi8 inverted microscope with a 63x objective
394 (oil immersion, NA=1.4, Hamamatsu Orca Flash 2.0 camera) and at room temperature (22-25°C).
395 To reduce autofluorescence during imaging, the culture medium was replaced with Live Imaging
396 Solution (Thermo Fisher A14291DJ). Culture media was not replaced for imaging cells in
397 Nocodazole, DMSO, and osmo+ to enable measurement of MT dynamics in the chosen media.
398 For EB1-GFP imaging, an image (exposure time 500 ms) was taken every 2 seconds for 70-150
399 frames depending on sample bleaching. When imaging both EB1-GFP and Jupiter-mcherry
400 simultaneously, one image was taken every 3 seconds for 100 frames (exposure 500ms). Lamp
401 intensity was set to the lowest level that enabled visual identification of labels.

402 ***p150 antibody staining***

403 24 hours after plating, the cells were treated with 5µM of Celltracker™ (Invitrogen C2925) dye
404 for 30 minutes to label cells in green. Subsequently, cells were fixed in pre-warmed 4%
405 paraformaldehyde (PFA) (pH 7.2, 26°C) for 50 minutes. Post-fixation, the cells were washed in
406 PBS once and then incubated with mouse alpha-tubulin 1:1000 (Abcam ab7291) and rabbit
407 glued/p150 antibody 1:500 (gift from the St Johnston laboratory, (Nieuwburg et al., 2017))
408 diluted in PBST (2x phosphate-buffered saline (PBS, Oxoid BR0014G) tablets in 400ml H2O + 1.2

409 ml Triton X-100) + 0.01 g/ml bovine serum albumin at 4°C overnight (~14h). After two quick
410 washes in PBS, the cells were incubated with the secondary antibodies Alexa Fluor 647 (far-red,
411 Thermo Fisher A-21236) and 405 (blue, Thermo Fisher A-31556) for 1.5 hours at room
412 temperature. After another two quick PBS washes, the cells were mounted in Fluoromount
413 (Thermo Fisher 00-4958-02) and imaged.

414 Images were analysed by drawing a line along axon processes from the base of the axon to its tip
415 in the tubulin channel. The intensity profiles for all 3 channels (p150, tubulin, and Celltracker)
416 were extracted and normalized by their respective median values, and the p150 channel was
417 subsequently divided by the normalised Celltracker channel and the data binned in bins of 10 µm.
418 Finally, the resulting binned *p150-RNAi* p150 profiles were normalized by the mean fluorescence
419 of the respective *wild-type* control p150 fluorescence. The resulting profiles (per axon) were then
420 pooled over all biological replicates and plotted in *Mathematica*. See **Error! Reference source**
421 **not found.** for a single cell workflow example.

422 ***EB1-GFP dynamics***

423 Kymographs of EB1-GFP tracks in *Drosophila melanogaster* axons were generated by first using
424 the Neurite Tracer plugin in ImageJ to draw lines along axons or dendrites from the centre of the
425 cell body to the farthest EB1-GFP comet signal, i.e. the distalmost growth event (Pool et al., 2008).
426 Subsequently a custom *Mathematica* (https://wolfram.com) algorithm automatically generated
427 kymographs from these lines by plotting the average pixel intensity of 3 adjacent pixels into rows
428 of an image for each frame. The resulting image was then smoothed with a Gaussian kernel of
429 size 3 and wavelet filtered to remove noise. Kymographs were analyzed with *KymoButler* and

430 subsequently post processed in *MATLAB* (https://mathworks.com). Tracks were removed in case:
431 (i) they displaced less than 2 pixels along the x-axis, (ii) they were slower than 1.5 µm/min, (iii)
432 they were faster than 20 µm/min, and (iv) they were visible for less than 4 frames. Additionally,
433 control experiments and their corresponding treatment condition were discarded if the control
434 axons exhibited a mean orientation below 0.8 or average growth velocities below 2 µm/min. To
435 account for outlier comets, the distance from the axon tip was calculated as the distance from
436 the 0.95 quantile EB1-GFP comet.

437 MT -end polymerisation is much slower than +end polymerisation (Strothman et al., 2019). Since
438 we observed similar growth velocities of cell body-directed and tip-directed MT growth, we are
439 confident that we measured +end out MT growth events in both directions rather than -end
440 growth.

441 Note that, mature *D. melanogaster* dendrites *in vivo* exhibit a mixed MT orientation (Stone et al.,
442 2008). However, we cultured neurons only up to 48h which might be too short to form fully
443 developed dendrites and our minimal cell culture medium is likely lacking growth factors that
444 would enable further differentiation to form fully -end out dendrites. Additionally, vertebrate
445 dendrites also appear to acquire their characteristic orientation over time (Baas et al., 1989).

446 ***Jupiter-mcherry & EB1-GFP***

447 Kymographs were prepared as for imaging EB1-GFP only (i.e. using Neurite Tracer). Individual
448 shrinkage events were extracted by hand from the resulting kymographs using the ROI tool in
449 *ImageJ* (https://imagej.net). The tracks were then analysed and plotted with *MATLAB* and

450 *Mathematica*. Measuring MT shrinkage dynamics was only possible in regions of low tubulin
451 content, e.g., near the axon tip. We implicitly assumed that MT shrinkage depends neither on MT
452 orientation nor on its position along the axon. However, experimental evidence suggests that a
453 decrease in MT growth length correlates with an increase in shrinkage length (Vasquez et al.,
454 2017), indicating that we likely overestimated MT lengths further away from the axon tip,
455 therefore underestimating the difference between +end out MTs at the tip and those further
456 away from it.

457 ***Statistics***

458 For comparing two groups the Wilcoxon rank sum test was used as implemented in MATLAB
459 (https://www.mathworks.com/help/stats/ranksum.html). The standard error of the mean
460 (s.e.m.) was calculated as $s.e.m. = \sigma/\sqrt{n}$. Here σ is the standard deviation of the sample and n
461 is the number of samples. The 95% confidence interval was calculated by median bootstrapping
462 with 10000 random samples from the distribution. Biological replicates are experiments
463 conducted on different days with different larvae and reagents. We used the Kruskal Wallis test
464 (https://uk.mathworks.com/help/stats/kruskalwallis.html) to compare several samples,
465 followed by a Dunn Sidak post hoc test.

466 ***Solution of the 2-state master equation***

467 We assumed that MTs can either grow or shrink, and each of these two states (g and s in short)
468 has a probability distribution that depends on MT length l and time t ($p_g(l,t)$ and $p_s(l,t)$). MTs
469 can furthermore stop growing and start shrinking with rate $f_g = 1/t_g$ (t_g being the average MT

growth time) and stop shrinking to start growing with rate $f_s = 1/t_s$ (t_s being the average MT shrinkage time). Furthermore, MTs are assumed to grow with velocity v_g and shrink with velocity v_s, while they are in the growing- or shrinking- state, respectively. Writing this as a master equation yields:

$$\frac{d}{dt} p_s(l,t) = f_g\, p_g(l,t) - f_s\, p_s(l,t)$$

$$\frac{d}{dt} p_g(l,t) = f_s\, p_s(l,t) - f_g\, p_g(l,t)$$

To solve this set of partial differential equations consider the following Fourier transformation of $p_s(l,t)$ and $p_g(l,t)$:

$$p_{s,g}(l,t) = \int dk\, d\omega\;\, e^{i\omega t - ikl}\, \tilde{p}_{s,g}(\omega,k)$$

Substituting in the 2-state master equation yields:

$$0 = \int dk\, d\omega\, e^{i\omega t - ikx} \left[\left(i\omega + f_g - ikv_g\right) \tilde{p}_g(\omega,k) - f_s\, \tilde{p}_s(\omega,k) \right]$$

$$0 = \int dk\, d\omega\, e^{i\omega t - ikx} \left[\left(i\omega + f_s + ikv_s\right) \tilde{p}_s(\omega,k) - f_g\, \tilde{p}_g(\omega,k) \right]$$

Which can be written as a matrix equation:

$$0 = \begin{pmatrix} i\omega + f_g - ikv_g & -f_s \\ -f_g & i\omega + f_s + ikv_s \end{pmatrix} \begin{pmatrix} \tilde{p}_g(\omega,k) \\ \tilde{p}_s(\omega,k) \end{pmatrix}$$

This equation only has non-zero solutions for $\tilde{p}_g$ and $\tilde{p}_s$ if the matrix determinant is equal to zero:

$$0 = det\begin{pmatrix} i\omega + f_g - ikv_g & -f_s \\ -f_g & i\omega + f_s + ikv_s \end{pmatrix} = \left(i\omega + f_g - ikv_g\right)(i\omega + f_s + ikv_s) + f_g\, f_s$$

This equation can be written as a dispersion relation:

$$\omega(k) = \overbrace{\left(\frac{f_s}{f_s + f_g} v_g - \frac{f_g}{f_s + f_g} v_s\right)}^{=\bar{v}} k + i \overbrace{\left(\frac{f_s\, f_g (v_g + v_s)^2}{(f_g + f_s)^3}\right)}^{=\bar{D}} k^2 + O(k^3) = \bar{v}\, k + i\, \bar{D}\, k^2 + O(k^3)$$

For large times t both ω and k are small so that we can drop terms of the order of k^3. The dispersion relation is then the same as for a diffusion advection process with drift velocity $\bar{v}$ and Diffusion coefficient $\bar{D}$. For $\bar{v} > 0$ the system will evolve like a diffusion advection process in which MTs would have no average length so that they will become as long as the system allows, i.e. their growth is "unbounded".

For $\bar{v} < 0$, MTs will exhibit an average length that depends on their dynamic parameters which can be calculated as follows: For large times, the overall probability to find a MT with length l at time t ($p(l,t) = p_g(l,t) + p_s(l,t)$) can be approximated by a modified diffusion-advection equation:

$$\frac{\partial}{\partial t} p(l,t) = \bar{D} \frac{\partial^2}{\partial l^2} p(l,t) + |\bar{v}| \frac{\partial}{\partial l} p(l,t)$$

The stationary state $\frac{\partial}{\partial t} p(l,t) = 0$ is thus found by:

$$0 = \frac{\partial^2}{\partial l^2} p(l) + \frac{|\bar{v}|}{\bar{D}} \frac{\partial}{\partial l} p(l)$$

The general solution to this partial differential equation is:

$$p(l) = C_1 \frac{\bar{D}}{|\bar{v}|}\, e^{-\frac{\bar{v}}{\bar{D}} l} + C_2$$

For $p(l,t)$ to be normalisable: $C_2 = 0$ and $C_1 = \left(\frac{|\bar{v}|}{\bar{D}}\right)^2$. So that:

$$p(l) = \frac{|\bar{v}|}{\bar{D}}\, e^{-\frac{\bar{v}}{\bar{D}} l}$$

This equation is a 2-state master equation that equates the rate change of a probability to be in one state (i.e. dp_s/dt) to the outflow ($-f_s p_s$,i.e. the likelihood of a shrinking microtubule to start growing) and the inflow ($f_g p_g$,i.e. the likelihood of a growing microtubule to start shrinking) into that state. With $dp/dt = \partial l/\partial t\, \partial p/\partial l = v\, \partial p/\partial l$ we can write:

$$\frac{\partial}{\partial t} p_s(l,t) = f_g\, p_g(l,t) - f_s\, p_s(l,t) + v_s \frac{\partial}{\partial l} p_s(l,t)$$

$$\frac{\partial}{\partial t} p_g(l,t) = f_s\, p_s(l,t) - f_g\, p_g(l,t) - v_g \frac{\partial}{\partial l} p_g(l,t)$$

Finally, one can calculate the average MT length l_{MT} as the expectation value of the length:

$$l_{MT} \equiv \langle l \rangle = \int_0^\infty dl\;\, l\, p(l) = \frac{\bar{D}}{|\bar{v}|} = \frac{f_s\, f_g (v_g + v_s)^2}{\left(f_g + f_s\right)^2 (v_s f_g - v_g f_s)}$$

For $v_s/v_g \approx 1$, $f_s/f_g \approx 1$, and $d = v/f$ the quadratic terms can be Taylor expanded to yield:

$$l_{MT} \approx \frac{v_g v_s}{\left(v_s f_g - v_g f_s\right)} = \frac{d_g d_s}{d_s - d_g}$$

515 **Analytical fit to estimate MT growth per cycle based on immunostainings**

516 The p150 fluorescence profiles were calculated as described in the section on "p150 antibody
517 staining". Subsequently, an exponential function, $p150(x) = b + e^{-s(x-x_0)}$, was fitted to the
518 first 12 bins of the data (corresponds to up until 120 µm from the tip). Here b, s, and x_0 are fitting
519 parameters with units: [b]=A.U., [s]=1/um, [x_0]=um. Next, we assumed that $d_g(x) =$
520 $A\, p150(x)^{\alpha}$, i.e. MT growth per cycle is a simple power law in the p150 fluorescence intensity.
521 *A* and α are fitting parameters and their values are shown in **Error! Reference source not found.**.
522 The expected growth length per cycle for a MT that starts growing at position x towards (1) or
523 away (-1) from the cell body can be approximated as:

524 $$d_g(x, sign) = 0.5\left(d_g\left(sign\ d_g(x) + x\right) + d_g(x)\right)$$

525 Here we assumed that the average length added to a MT during growth is the mean between the
526 average expected growth length at start and end position of the MT +end. This function was
527 subsequently fitted to the growth length data presented in **FIGURE 1F.** To do so, the experimental
528 data was first binned in bins of size 10 µm (like the staining data). Then we calculated the integral
529 of $d_g(x, sign)$ over each bin for each direction of growth and minimised the squared difference
530 to the experimental results by varying A and α. Note that we assumed that MTs that grow way
531 from the tip have to be at least 4 µm away from it (average MT length (Yu and Baas, 1994)) and
532 that MTs that grow into the tip may penetrate it by 2 µm.

533 **MT sliding simulations**

534 Details of the simulation can be found in (Jakobs et al., 2020). We here present a brief description
535 that focusses on the novel way in which new MTs are added during the simulation. MTs were
536 arranged with their long axis along the *x*-axis of a Cartesian coordinate system and their centers
537 on a hexagonal lattice in the $y - z$ plane. For simplicity all MTs were assumed to have the same
538 length, l_{MT} = 4µm. The inter-MT spacing in the y - z plane (~ 30 nm) was assumed to allow
539 individual molecular motors (here, cytoplasmic dynein) to intervene between adjacent filaments
540 and cross-link them with their respective 'cargo' or 'walking' domains. The simulation was
541 initialized with 10 randomly oriented MTs that were randomly distributed on a hexagonal lattice
542 of lenght 6 µm. New MTs were added to the system depending on the chosen nucleation model:

543 1. Sliding only: MTs were added at random locations with random orientation every 1100
544 seconds (~18 minutes). The time was optimised to yield axons of approximately the same
545 length as cultured ones.
546 2. Sliding and templating: MTs were added at random locations every 1100 seconds. The
547 likelihood of being +end out was calculated by counting the number and orientation of
548 MTs at the location (the center of the MT) in which the MT is added. Then the number of
549 +end out MTs was divided by the total number of MTs to calculate the probability of
550 getting a +end out MT. Finally a random number is drawn between 0 and 1 to determine
551 the orientation of the added MT.
552 3. Templating Only: Same as above except that the directionality of the movement of
553 molecular motors along the MTs was eliminated. When MT overlaps became occupied

554 with motors, the motors' gliding direction towards the +end or the –end of the MTs was
555 chosen at random. Note that this is a highly artificial setting that solely removes the
556 sorting effect of microtubule sliding.

557 4. Sliding and unbounded growth: A random location along the axon was chosen and a
558 random MT orientation (50/50 +end out/-end out) introduced every 435 seconds. As not
559 every MT nucleated in this model, the rate of influx was selected to be higher to enable
560 the same axon growth behaviour. Subsequently, we calculated the likelihood of
561 exhibiting unbounded growth for a MT with the randomly selected orientation and
562 location. To do so, we first calculated the average added length per growth cycle in 10µm
563 bins (distance from the axon tip and separately for +end out and -end out MTs) for each
564 axon in the dataset presented in **FIGURE 1A-G**. For each bin we then queried whether
565 growth was bounded (added length below 2.2µm) or unbounded. The likelihood of
566 unbounded growth was calculated for each bin by counting the number of axons that
567 exhibited unbounded growth in the bin and dividing that number by all axons.
568 Subsequently, two exponential functions were fitted to the +end out and -end out MT
569 data respectively to determine a function that gives the likelihood of unbounded growth
570 for +end out and -end out MTs as a function of distance from the axon tip. Finally, the
571 random location and the predetermined orientation were used to look up the likelihood
572 of unbounded growth and the MT was assumed to have nucleated successfully when a
573 randomly drawn number [0,1] was smaller than that likelihood.

574 5. Unbounded growth only: Same as above but molecular motors were again assumed to
575 not have a preferred direction as in 3.

576 6. Sliding, templating and unbounded growth: A random location along the axon was
577 chosen every 435 seconds and its orientation likelihood calculated as in 2. Subsequently,
578 the unbounded growth likelihood was calculated as in 3. MTs only successfully entered
579 the system if exhibiting unbounded growth.

580 MTs that were neighbours on the *y-z* plane and overlapping along the x-axis were crosslinked by
581 cytoplasmic dynein. For simplicity and due to the tight packing of MTs in the bundle, only motion
582 in parallel to the *x*-axis was considered. MT velocities were determined by solving a set of force
583 balance equations that characterize dynein interaction with the MTs, detailed in (Jakobs et al.,
584 2020). Furthermore, the left boundary was a leaky spring; MTs that moved into the left boundary
585 were subject to a force of 50 pN/µm and were able to leave the axon with a fixed rate per MT
586 (0.00024/sec). The rate was adjusted to lead to axons of 50 µm in length after approximately 24
587 hours simulation time. The right boundary was a constant force of 50 pN as described in (Jakobs
588 et al., 2020).

589 Axons were simulated for 50001 iterations (~28 hours) and all results averaged over 50 separate
590 simulations. Simulation parameters were as follows:

Symbol	**Description**	**Value**	**Reasoning**
χ	Fraction of overlapping MTs that are cross linked	1	We previously explored how changing χ affects MT sliding (Jakobs et al., 2020; 2015). In this manuscript we simply wanted to explore the effect of different MT addition

			models on MT orientation in which we fixed the value at 1.
λ	Number of motors bound in an overlapping region [#/µm]	5	We quantified (by eye) the number of MT crosslinks in EM images of axons (Hirokawa et al., 2010) which was approximately 3 per 100 nm.
l_{MT}	MT lengths [µm]	4 µm	Average MT lengths in axons measured in (Yu and Baas, 1994)
ξ	Drag coefficient of the axoplasm	1 pN sec / µm^2	Same coefficient used in (Oelz et al., 2018)
f_s	Dynein stall force	1.4 pN	Same coefficient used in (Oelz et al., 2018)
v_0	Dynein free velocity	0.86 µm/sec	Same coefficient used in (Oelz et al., 2018)
dt	Simulation timestep per iteration	2 seconds	As we showed previously (Jakobs et al., 2020; 2015), this value is a good choice to ensure smooth movements of MTs during the simulation.

591

592 **Acknowledgements:** We would like to thank Eva Pillai, Dennis Bray, Michael Takla, and Kevin
593 Chalut for inspiring discussions and proofreading, Andreas Prokop and Cristina Melero for
594 teaching *Drosophila* dissection techniques, and Sarah Bray, Dmitry Nashchekin, Daniel St
595 Johnston, and Nick Brown for providing *Drosophila* strains, laboratory space and a great
596 atmosphere to work in. The authors acknowledge funding from the Wellcome Trust (PhD
597 studentship 109145/Z/15/Z to MAHJ), the UK Biotechnology and Biological Sciences Research
598 Council (Research Grant BB/N006402/1 to KF), the European Research Council (Consolidator
599 Award 772426 to KF), and the Alexander von Humboldt Foundation (Alexander von Humboldt
600 Professorship to KF).

601 **Competing interests:** AZ declares no competing interests, MAHJ and KF are shareholders of
602 deepMirror (https://deepmirror.ai), a company that, amongst other products, sells custom
603 interfaces of the freeware *KymoButler*.

604 **Supplementary Information:**

605 Figures S1-S9

606 **References**

607 Ahmad, F.J., Echeverri, C.J., Vallee, R.B., and Baas, P.W. (1998). Cytoplasmic dynein and dynactin are required for
608 the transport of microtubules into the axon. J Cell Biol *140*, 391–401.

609 Baas, P.W., BLACK, M.M., and BANKER, G.A. (1989). Changes in microtubule polarity orientation during the
610 development of hippocampal neurons in culture. J Cell Biol *109*, 3085–3094.

611 Baas, P.W., and Lin, S. (2011). Hooks and comets: The story of microtubule polarity orientation in the neuron.
612 Developmental Neurobiology *71*, 403–418.

613 Bergstralh, D.T., Lovegrove, H.E., and St Johnston, D. (2015). Lateral adhesion drives reintegration of misplaced
614 cells into epithelial monolayers. Nat Cell Biol *17*, 1497–1503.

615 BRAY, D., Money, N.P., Harold, F.M., and Bamburg, J.R. (1991). Responses of growth cones to changes in osmolality
616 of the surrounding medium. J Cell Sci *98 (Pt 4)*, 507–515.

617 Bulgakova, N.A., Grigoriev, I., Yap, A.S., Akhmanova, A., and Brown, N.H. (2013). Dynamic microtubules produce an
618 asymmetric E-cadherin-Bazooka complex to maintain segment boundaries. J Cell Biol *201*, 887–901.

619 Bulgakova, N.A., Klapholz, B., and Brown, N.H. (2012). Cell adhesion in Drosophila: versatility of cadherin and
620 integrin complexes during development. Current Opinion in Cell Biology *24*, 702–712.

621 Conde, C., and Cáceres, A. (2009). Microtubule assembly, organization and dynamics in axons and dendrites. Nat.
622 Rev. Neurosci. *10*, 319–332.

623 del Castillo, U., Winding, M., Lu, W., Gelfand, V.I. (2015). Interplay between kinesin-1 and cortical dynein during
624 axonal outgrowth and microtubule organization in Drosophila neurons. eLife Sciences *4*, e10140.

625 Dogterom, M., and Leibler, S. (1993). Physical aspects of the growth and regulation of microtubule structures.
626 Phys. Rev. Lett. *70*, 1347–1350.

627 Dogterom, M., and Yurke, B. (1997). Measurement of the force-velocity relation for growing microtubules. Science
628 *278*, 856–860.

629 Egger, B., van Giesen, L., Moraru, M., and Sprecher, S.G. (2013). In vitro imaging of primary neural cell culture from
630 Drosophila. Nat Protoc *8*, 958–965.

631 Eng, H., Lund, K., and Campenot, R.B. (1999). Synthesis of beta-tubulin, actin, and other proteins in axons of
632 sympathetic neurons in compartmented cultures. Journal of Neuroscience *19*, 1–9.

633 Franze, K. (2020). Integrating Chemistry and Mechanics: The Forces Driving Axon Growth. Annu. Rev. Cell Dev. Biol.
634 *36*, 61–83.

635 Fukata, Y., Itoh, T.J., Kimura, T., Ménager, C., Nishimura, T., Shiromizu, T., Watanabe, H., Inagaki, N., Iwamatsu, A.,
636 Hotani, H., et al. (2002). CRMP-2 binds to tubulin heterodimers to promote microtubule assembly. Nat Cell Biol *4*,
637 583–591.

638 Gill, S.R., Schroer, T.A., Szilak, I., Steuer, E.R., Sheetz, M.P., and Cleveland, D.W. (1991). Dynactin, a conserved,
639 ubiquitously expressed component of an activator of vesicle motility mediated by cytoplasmic dynein. J Cell Biol
640 *115*, 1639–1650.

641 Heidemann, S.R., Landers, J.M., and Hamborg, M.A. (1981). Polarity orientation of axonal microtubules. J Cell Biol
642 *91*, 661–665.

643 Hirokawa, N., Niwa, S., and Tanaka, Y. (2010). Molecular Motors in Neurons: Transport Mechanisms and Roles in
644 Brain Function, Development, and Disease. Neuron *68*, 610–638.

645 Inagaki, N., Chihara, K., Arimura, N., Ménager, C., Kawano, Y., Matsuo, N., Nishimura, T., Amano, M., and Kaibuchi,
646 K. (2001). CRMP-2 induces axons in cultured hippocampal neurons. Nat. Neurosci. *4*, 781–782.

647 Jakobs, M.A.H., Franze, K., and Zemel, A. (2020). Mechanical Regulation of Neurite Polarization and Growth: A
648 Computational Study. Biophysical Journal *118*, 1914–1920.

649 Jakobs, M.A., Dimitracopoulos, A., and Franze, K. (2019). KymoButler, a deep learning software for automated
650 kymograph analysis. eLife Sciences *8*, 168.

651 Jakobs, M., Franze, K., and Zemel, A. (2015). Force Generation by Molecular-Motor-Powered Microtubule Bundles;
652 Implications for Neuronal Polarization and Growth. Front Cell Neurosci *9*, 441.

653 Kapitein, L.C., and Hoogenraad, C.C. (2011). Which way to go? Cytoskeletal organization and polarized transport in
654 neurons. Mol. Cell. Neurosci. *46*, 9–20.

655 Karki, S., and Holzbaur, E.L. (1995). Affinity chromatography demonstrates a direct binding between cytoplasmic
656 dynein and the dynactin complex. J. Biol. Chem. *270*, 28806–28811.

657 Kuijpers, M., and Hoogenraad, C.C. (2011). Centrosomes, microtubules and neuronal development. Mol. Cell.
658 Neurosci. *48*, 349–358.

659 Lazarus, J.E., Moughamian, A.J., Tokito, M.K., and Holzbaur, E.L.F. (2013). Dynactin subunit p150(Glued) is a
660 neuron-specific anti-catastrophe factor. PLoS Biol. *11*, e1001611.

661 Liang, X., Kokes, M., Fetter, R.D., Sallee, M.D., Moore, A.W., Feldman, J.L., and Shen, K. (2020). Growth cone-
662 localized microtubule organizing center establishes microtubule orientation in dendrites. eLife Sciences *9*, 308.

663 Lowery, L.A., and Van Vactor, D. (2009). The trip of the tip: understanding the growth cone machinery. Nat. Rev.
664 Mol. Cell Biol. *10*, 332–343.

665 Ma, Y., Shakiryanova, D., Vardya, I., and Popov, S.V. (2004). Quantitative Analysis of Microtubule Transport in
666 Growing Nerve Processes. Current Biology *14*, 725–730.

667 Mattie, F.J., Stackpole, M.M., Stone, M.C., Clippard, J.R., Rudnick, D.A., Qiu, Y., Tao, J., Allender, D.L., Parmar, M.,
668 and Rolls, M.M. (2010). Directed microtubule growth, +TIPs, and kinesin-2 are required for uniform microtubule
669 polarity in dendrites. Curr. Biol. *20*, 2169–2177.

670 Millecamps, S., and Julien, J.-P. (2013). Axonal transport deficits and neurodegenerative diseases. Nature
671 Publishing Group *14*, 161–176.

672 Molines, A.T., Lemière, J., Edrington, C.H., Hsu, C.-T., Steinmark, I.E., Suhling, K., Goshima, G., Holt, L.J., Brouhard,
673 G.J., and Chang, F. (2020). Physical properties of the cytoplasm modulate the rates of microtubule growth and
674 shrinkage. bioRxiv *265*, 2020.10.27.352716.

675 Morland, C., Pettersen, M.N., and Hassel, B. (2016). Hyperosmolar sodium chloride is toxic to cultured neurons and
676 causes reduction of glucose metabolism and ATP levels, an increase in glutamate uptake, and a reduction in
677 cytosolic calcium. NeuroToxicology *54*, 34–43.

678 Morrison, E.E., Moncur, P.M., and Askham, J.M. (2002). EB1 identifies sites of microtubule polymerisation during
679 neurite development. Brain Res Mol Brain Res *98*, 145–152.

680 Moughamian, A.J., and Holzbaur, E.L.F. (2012). Dynactin is required for transport initiation from the distal axon.
681 Neuron *74*, 331–343.

682 Mukherjee, A., Jenkins, B., Fang, C., Radke, R.J., Banker, G., and Roysam, B. (2011). Automated kymograph analysis
683 for profiling axonal transport of secretory granules. Medical Image Analysis *15*, 354–367.

684 Mukherjee, A., Brooks, P.S., Bernard, F., Guichet, A., and Conduit, P.T. (2020). Microtubules originate
685 asymmetrically at the somatic golgi and are guided via Kinesin2 to maintain polarity within neurons. eLife Sciences
686 *9*, 2191.

687 Nguyen, M.M., McCracken, C.J., Milner, E.S., Goetschius, D.J., Weiner, A.T., Long, M.K., Michael, N.L., Munro, S.,
688 and Rolls, M.M. (2014). Γ-tubulin controls neuronal microtubule polarity independently of Golgi outposts. Mol.
689 Biol. Cell *25*, 2039–2050.

690 Nieuwburg, R., Nashchekin, D., Jakobs, M., Carter, A.P., Khuc Trong, P., Goldstein, R.E., and St Johnston, D. (2017).
691 Localised dynactin protects growing microtubules to deliver oskar mRNA to the posterior cortex of the Drosophila
692 oocyte. eLife Sciences *6*, 711.

693 Oelz, D.B., del Castillo, U., Gelfand, V.I., and Mogilner, A. (2018). Microtubule Dynamics, Kinesin-1 Sliding,
694 and Dynein Action Drive Growth of Cell Processes. Biophysical Journal *115*, 1614–1624.

695 Pilling, A.D., Horiuchi, D., Lively, C.M., and Saxton, W.M. (2006). Kinesin-1 and Dynein are the primary motors for
696 fast transport of mitochondria in Drosophila motor axons. Mol. Biol. Cell *17*, 2057–2068.

697 Plough, H.H., and Ives, P.T. (1935). Induction of Mutations by High Temperature in Drosophila. Genetics *20*, 42–69.

698 Pool, M., Thiemann, J., Bar-Or, A., and Fournier, A.E. (2008). NeuriteTracer: a novel ImageJ plugin for automated
699 quantification of neurite outgrowth. Journal of Neuroscience Methods *168*, 134–139.

700 Rao, A.N., Patil, A., Black, M.M., Craig, E.M., Myers, K.A., Yeung, H.T., and Baas, P.W. (2017). Cytoplasmic Dynein
701 Transports Axonal Microtubules in a Polarity-Sorting Manner. Cell Rep *19*, 2210–2219.

702 Roostalu, J., Thomas, C., Cade, N.I., Kunzelmann, S., Taylor, I.A., and Surrey, T. (2020). The speed of GTP hydrolysis
703 determines GTP cap size and controls microtubule stability. eLife Sciences *9*.

704 Sanchez-Soriano, N., Gonçalves Pimentel, C., Beaven, R., Haessler, U., Ofner Ziegenfuss, L., Ballestrem, C., and
705 Prokop, A. (2010). Drosophila growth cones: A genetically tractable platform for the analysis of axonal growth
706 dynamics. Developmental Neurobiology *70*, 58–71.

707 Sánchez-Huertas, C., Freixo, F., Viais, R., Lacasa, C., Soriano, E., and Lüders, J. (2016). Non-centrosomal nucleation
708 mediated by augmin organizes microtubules in post-mitotic neurons and controls axonal microtubule polarity. Nat
709 Commun *7*, 12187.

710 Schindelin, J., Arganda-Carreras, I., Frise, E., Kaynig, V., Longair, M., Pietzsch, T., Preibisch, S., Rueden, C., Saalfeld,
711 S., Schmid, B., et al. (2012). Fiji: an open-source platform for biological-image analysis. Nat. Methods *9*, 676–682.

712 Seetapun, D., and Odde, D.J. (2010). Cell-length-dependent microtubule accumulation during polarization. Curr.
713 Biol. *20*, 979–988.

714 Shimada, Y., Yonemura, S., Ohkura, H., Strutt, D., and Uemura, T. (2006). Polarized Transport of Frizzled along the
715 Planar Microtubule Arrays in Drosophila Wing Epithelium. Dev. Cell *10*, 209–222.

716 Stepanova, T., Slemmer, J., Hoogenraad, C.C., Lansbergen, G., Dortland, B., De Zeeuw, C.I., Grosveld, F., van
717 Cappellen, G., Akhmanova, A., and Galjart, N. (2003). Visualization of microtubule growth in cultured neurons via
718 the use of EB3-GFP (end-binding protein 3-green fluorescent protein). J. Neurosci. *23*, 2655–2664.

719 Stone, M.C., Roegiers, F., and Rolls, M.M. (2008). Microtubules have opposite orientation in axons and dendrites of
720 Drosophila neurons. Mol. Biol. Cell *19*, 4122–4129.

721 Strothman, C., Farmer, V., Arpağ, G., Rodgers, N., Podolski, M., Norris, S., Ohi, R., and Zanic, M. (2019). Microtubule
722 minus-end stability is dictated by the tubulin off-rate. J Cell Biol *218*, 2841–2853.

723 Tas, R.P., Chazeau, A., Cloin, B.M.C., Lambers, M.L.A., Hoogenraad, C.C., and Kapitein, L.C. (2017). Differentiation
724 between Oppositely Oriented Microtubules Controls Polarized Neuronal Transport. Neuron *96*, 1264–1271.e1265.

725 Twelvetrees, A.E., Pernigo, S., Sanger, A., Guedes-Dias, P., Schiavo, G., Steiner, R.A., Dodding, M.P., and Holzbaur,
726 E.L.F. (2016). The Dynamic Localization of Cytoplasmic Dynein in Neurons Is Driven by Kinesin-1. Neuron *90*, 1000–
727 1015.

728 van Beuningen, S.F.B., Will, L., Harterink, M., Chazeau, A., van Battum, E.Y., Frias, C.P., Franker, M.A.M., Katrukha,
729 E.A., Stucchi, R., Vocking, K., et al. (2015). TRIM46 Controls Neuronal Polarity and Axon Specification by Driving the
730 Formation of Parallel Microtubule Arrays. Neuron *88*, 1208–1226.

731 Vasquez, R.J., Howell, B., Yvon, A.M., Wadsworth, P., and Cassimeris, L. (2017). Nanomolar concentrations of
732 nocodazole alter microtubule dynamic instability in vivo and in vitro. Mol. Biol. Cell *8*, 973–985.

733 Voelzmann, A., Hahn, I., Pearce, S.P., Sanchez-Soriano, N., and Prokop, A. (2016). A conceptual view at microtubule
734 plus end dynamics in neuronal axons. Brain Res. Bull.

735 Waterman-Storer, C.M., Karki, S.B., Kuznetsov, S.A., Tabb, J.S., Weiss, D.G., Langford, G.M., and Holzbaur, E.L.
736 (1997). The interaction between cytoplasmic dynein and dynactin is required for fast axonal transport. Pnas *94*,
737 12180–12185.

738 Yannoni, Y.M., and White, K. (1997). Association of the neuron-specific RNA binding domain-containing protein
739 ELAV with the coiled body in Drosophila neurons. Chromosoma *105*, 332–341.

740 Yau, K.W., Schätzle, P., Tortosa, E., Pagès, S., Holtmaat, A., Kapitein, L.C., and Hoogenraad, C.C. (2016a). Dendrites
741 In Vitro and In Vivo Contain Microtubules of Opposite Polarity and Axon Formation Correlates with Uniform Plus-
742 End-Out Microtubule Orientation. J. Neurosci. *36*, 1071–1085.

743 Yau, K.W., Schätzle, P., Tortosa, E., Pagès, S., Holtmaat, A., Kapitein, L.C., and Hoogenraad, C.C. (2016b). Dendrites
744 In Vitro and In Vivo Contain Microtubules of Opposite Polarity and Axon Formation Correlates with Uniform Plus-
745 End-Out Microtubule Orientation. J. Neurosci. *36*, 1071–1085.

746 Yu, W., and Baas, P.W. (1994). Changes in microtubule number and length during axon differentiation. Journal of
747 Neuroscience *14*, 2818–2829.

748 Yu, W., Qiang, L., Solowska, J.M., Karabay, A., Korulu, S., and Baas, P.W. (2008). The Microtubule-severing Proteins
749 Spastin and Katanin Participate Differently in the Formation of Axonal Branches. Mol. Biol. Cell *19*, 1485–1498.

750

751 **Figures**

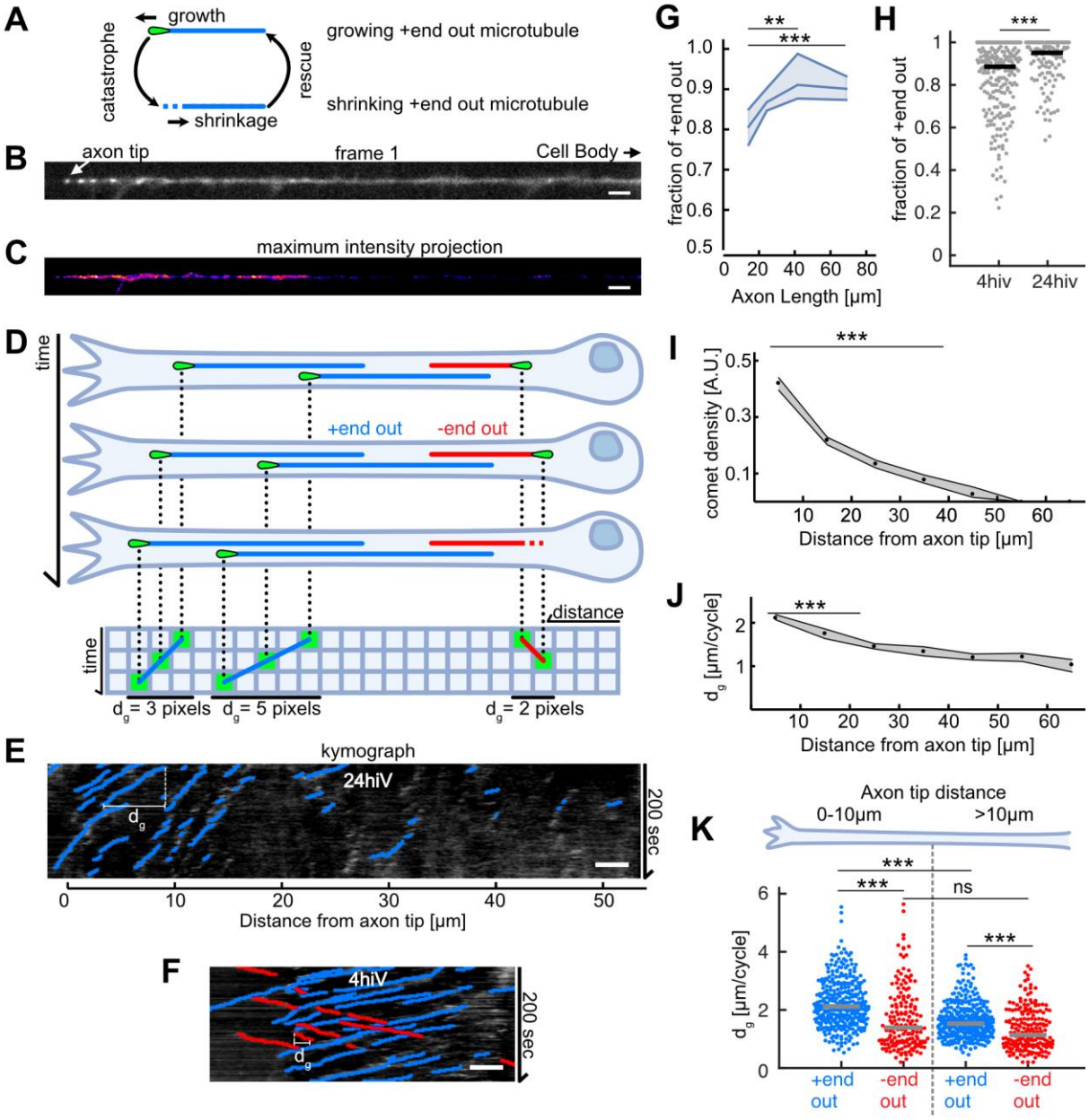

752

753 **Figure 1: Axonal MT orientation increases over time and MT growth is enhanced at axon tips. (A)** Schematic
754 depicting the MT growth and shrinkage cycle. MTs grow until they undergo a catastrophe, which initiates MT
755 shrinkage, and they start growing again after a rescue event. During growth (but not during shrinkage), EB1 localizes
756 to MT tips. **(B)** First frame of a live cell imaging movie of axonal EB1-GFP dynamics. Bright dots represent individual
757 EB1-GFP puncta, which label growing MT +ends. **(C)** Maximum intensity projection of a 200-second-long movie

758 depicting EB1-GFP dynamics in a *D melanogaster* axon. EB1-GFP density is increased towards the tip. **(D)** Schematic
759 showing how EB1-GFP live imaging movies were visualized and analysed using kymographs. The growing tips of +end
760 out MTs (blue) and -end out MTs (red) were fluorescently labelled with EB1-GFP (green tear drop shaped 'comets').
761 The same axon is shown at three different time points; MTs grow at their +end, where EB1-GFP is located. The axonal
762 intensity profiles of all time points are plotted underneath each other, resulting in a space-time grid called
763 'kymograph'. Connecting puncta between consecutive kymograph lines with blue/red lines yields the overall
764 displacement d_g for individual MT growth events. Note that the red -end out MT stops growing in the 2nd frame and
765 shrinks in the 3rd frame **(E)** Kymograph of an axon 24 hours post plating showing EB1-GFP dynamics analysed with
766 *KymoButler* (Jakobs et al., 2019). Lines with a positive slope (blue, left to right upwards) are MTs growing with their
767 +end towards the axon tip, lines with a negative slope (red, left to right downwards) are MTs growing away from the
768 tip. Horizontal bars indicate the growth lengths (d_g) for individual MT growth cycles. **(F)** Kymographs of axonal
769 processes expressing EB1-GFP analysed with *KymoButler* 4 hours post-plating **(G)** MT orientation as a function of
770 axon length. Longer axons exhibit a more pronounced +end out MT orientation ($p < 10^{-5}$, Kruskal Wallis test, **p <
771 0.01, ***p < 0.001 for pairwise comparisons, Dunn Sidak post hoc test). **(H)** MT orientation at 4 h.i.v and 24 h.i.v
772 (*hours in vitro*). MT orientation increased with time ($p < 10^{-4}$, Wilcoxon ranksum test). **(I)** EB1-GFP comet density as
773 a function of the distance from the axon tip. Most MT polymerization occurred near the advancing axon tip. (N Axons
774 = 353, 20 biological replicates from 20 different experiment days, $p < 10^{-20}$, Kruskal Wallis test, $p < 10^{-7}$ for pairwise
775 comparisons between bin 1 to 2,3, or 4, Dunn-Sidak post hoc test). Shown are median ± 95% confidence interval. **(J)**
776 Added length per MT growth cycle d_g as a function of distance from the axon tip. MTs grew longer in the vicinity of
777 the axon tip ($p < 10^{-20}$, Kruskal Wallis test, $p < 10^{-7}$ for pairwise comparisons of either bin 1 or 2 with any other bin,
778 Dunn-Sidak post hoc test). **(K)** d_g for +end out (blue) and -end out (red) MTs grouped for growth in the distalmost 10
779 µm of the axon tip, and further away than 10 µm from the axon tip. Each dot represents the average of one axon in
780 the respective region, grey lines indicate median values. With d_g 2.11 [2.04, 2.16] µm / cycle (bootstrapped median
781 [95% confidence interval]), +end out MTs near the axon tip grew significantly longer than -end out MTs (d_g =1.39
782 [1.27, 1.50] µm/cycle) and MTs located further away from the tip (d_g = 1.53 [1.47, 1.59] µm / cycle, +end out, d_g =
783 1.16 [1.03, 1.33] µm / cycle, -end out) (N = 346 (+end out close to tip), 343 (+end out away from tip), 177 (-end out

784 close to tip), 194 (-end out away from tip) axons), 20 biological replicates; $p < 10^{-30}$, Kruskal Wallis test followed by

785 Dunn-Sidak post hoc test; *** $p < 10^{-4}$). Scale bars: 3µm.

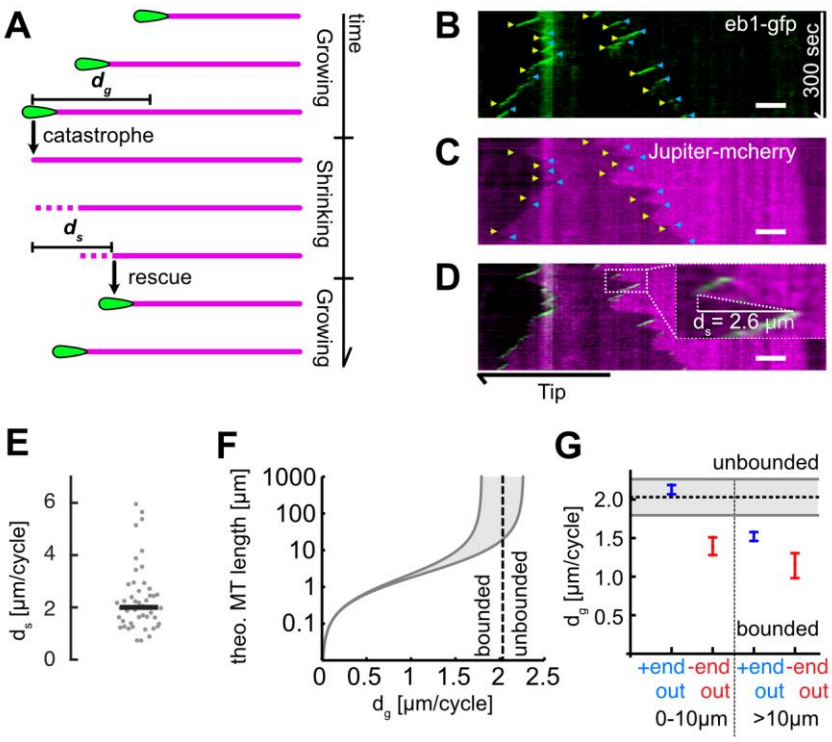

Figure 2: MT length depends on added length per growth cycle. (**A)** Schematic highlighting the assumptions of our two-state master equation model. MTs were assumed to occupy either a growing or shrinking state. During a growth cycle, the average MT length increases by d_g , during a shrinkage cycle, the MT length decreases by d_s . Additionally, MTs were able to stochastically switch between the two states as shown in **Figure 1A. (B-D)** Kymographs from a *D. melanogaster* axon that expressed **(B)** EB1-GFP (green) and **(C)** Jupiter-mCherry, a tubulin label (magenta). Individual MT shrinkage events, visible as **(C)** fluorescent edges and **(D)** dashed white lines in the kymograph, yielded MT shrinkage lengths per cycle d_s. Yellow and blue arrow heads in **B** & **C** indicate start and end points of an individual shrinkage event, and the inset in **D** highlights an individual shrinkage event. Scale bars: 3µm**. (E)** Average d_s values for N=47 axons (3 biological replicates; median: 2.03 [1.80, 2.26] µm (bootstrapped median [95% confidence]). **(F)** Plot of the estimated overall MT length l_{MT} as a function of d_g. The two solid black curves indicate the lower and upper bounds of the average MT lengths for a given d_g with d_s = 1.80 or 2.26 µm. One can separate two regimes, "unbounded" and "bounded" growth, separated by the dashed grey line. **(G)** Plot of d_g as a function of MT orientation and localisation showing median and 95% confidence intervals. +end out MTs close to the tip were

800 considerably more likely to exhibit unbounded growth than +end out MTs further away from the tip and -end out

801 MTs.

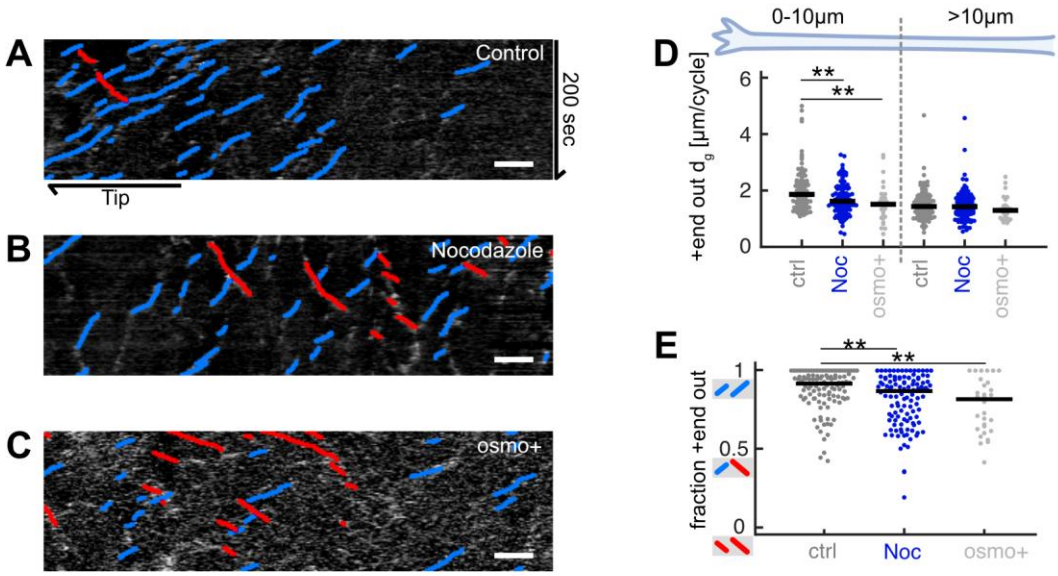

Figure 3: Decreasing MT growth leads to decreased axonal MT orientation. (A-C) Representative kymographs analysed with *KymoButler* (Jakobs et al., 2019) from axonal processes treated with (**A**) 0.025% DMSO (control) for 8h, **(B)** 5uM Nocodazole for 8h, **(C)** medium with increased osmolarity ("osmo+") for 22h. Growth of +end out MTs is shown as blue lines, -end MTs are red. Scale bars = 3µm. **(D)** Added MT lengths per growth cycle d_g of +end out MTs at the distalmost 10µm from the axon tip and further away for control (N = 107 axons from 5 biological replicates), nocodazole-treated axons (N = 116 axons from 3 biological replicates), and axons cultured in osmo+ medium (N = 30, 2 biological replicates). At the axon tip, MT lengths increased significantly less per growth cycle in axons treated with Nocodazole or osmo+ media than controls ($p < 10^{-4}$, Kruskal Wallis test, ** $p < 0.01$ for pairwise comparisons, Dunn-Sidak post hoc test). **(E)** The fraction of +end out MTs in the different groups. MT orientation was calculated by counting all MTs that grew away from the cell body (blue lines in kymographs) and dividing them by all growing MTs (blue and red) along the whole axons. This way, a kymograph with only blue lines gives a value of 1 while an equal number of blue and red lines yields a value of 0.5. MTs in axons treated with Nocodazole or osmo+ media were significantly less uniformly oriented than those in the control group, i.e., they contained a larger fraction of MTs pointing with their +ends toward the cell body (red lines in **(A-C)**) ($p < 10^{-4}$, Kruskal Wallis test, ** $p < 10^{-2}$ for pairwise comparisons, Dunn-Sidak post hoc test).

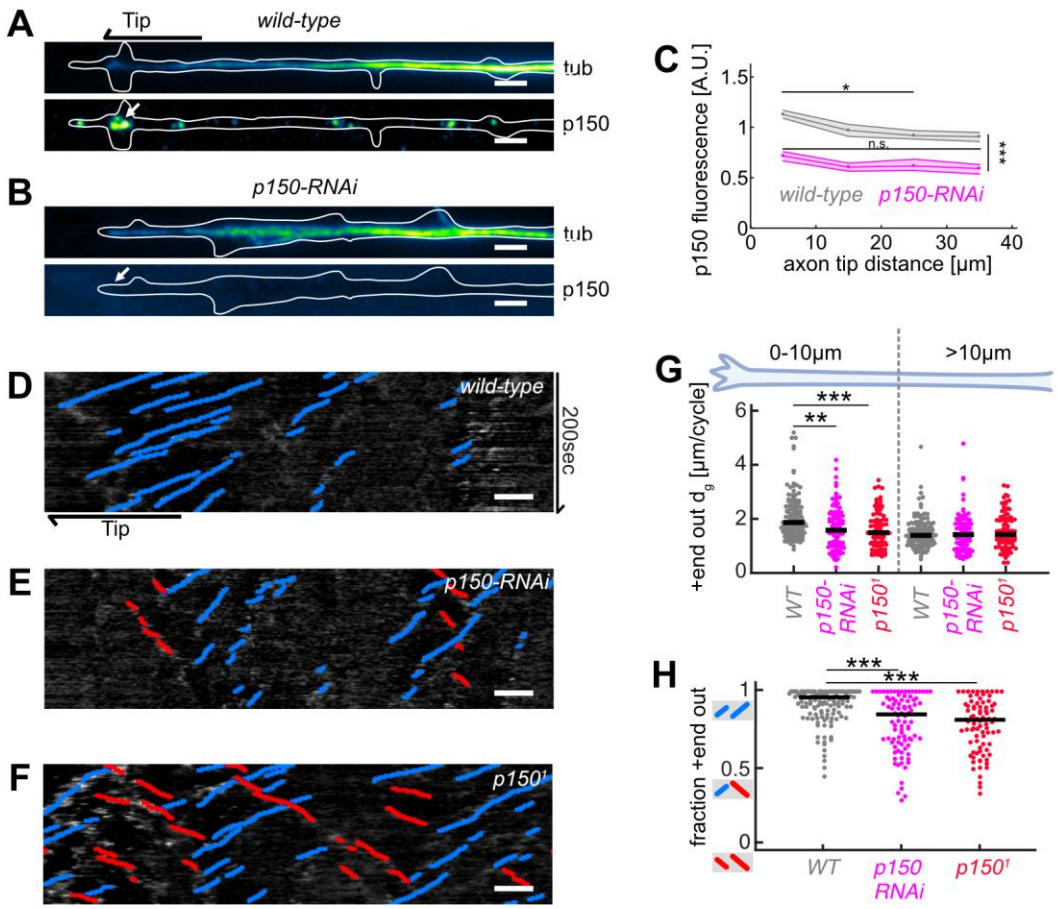

Figure 4: Abrogation of p150 function decreases MT growth and axonal MT orientation. (A-B) Tubulin (top) and normalized p150 (bottom) immunostaining of cultured *D. melanogaster* larvae axonal processes of **(A)** controls and **(B)** neurons expressing *elav-gal4* UAS-driven *p150-RNAi*. Large p150 puncta were found clustered around the axon tip (arrow) in controls **(A)** but not in *p150-RNAi* axons **(B)**. Scale bars = 2µm **(C)** Normalized p150 fluorescence intensity as a function of distance from the axon tip for *wild-type* axons (N = 83, 2 biological replicates) and *p150-RNAi* axons (N = 111, 2 biological replicates). Lines represent median ± 95% confidence intervals for *wild-type* (grey) and *p150-RNAi* (magenta). P150 fluorescence intensities changed along the axon ($p < 10^{-70}$; Kruskal Wallis test). In *wild-type* axons, p150 was enriched at the axon tip (* $p < 0.05$ between bin 1 and bin 3 or 4; pairwise comparisons with Dunn-Sidak post hoc test), but not in *p150-RNAi* expressing axons ($p > 0.05$ for all pairwise comparisons). Overall, p150 expression levels were diminished in *p150-RNAi* axons compared to *wild-type* (*** $p < 10^{-7}$ for any pairwise comparison between conditions). **(D-F)** *KymoButler* output for kymographs of EB1-GFP expressed in (**D**) a *wild-type*

831 axon, **(E)** an axon expressing p150-RNAi, and **(F)** an axon in a *p150^{1}/+* mutant background. Scale bars = 3 µm. Blue/red
832 lines represent MTs with +/-end out orientation, respectively. **(G)** +end out MT added length per growth cycle d_g for
833 *wild-type* (N = 85, 9 biological replicates), *p150-RNAi* (N = 34, 3 biological replicates), and *p150^{1}/+* (N = 83, 6 biological
834 replicates). At the axon tip, MT growth lengths were significantly decreased in both *p150-RNAi* and *p150^{1}* conditions
835 compared to controls ($p < 10^{-9}$, Kruskal Wallis test, ***$p < 0.001$, *$p < 0.05$, Dunn-Sidak post hoc test). **(H)** MT
836 orientation along the whole axon for *wild-type*, *p150-RNAi*, and *p150^{1}/+*. MTs were less uniformly oriented in both
837 *p150-RNAi* and *p150^{1}* axons ($p < 10^{-9}$, Kruskal Wallis test, *** $p < 10^{-5}$ for pairwise comparisons with Dunn-Sidak post
838 hoc test). Overall, axonal MT orientation was decreased after chemical, physical, and genetic perturbations of MT
839 growth.

840

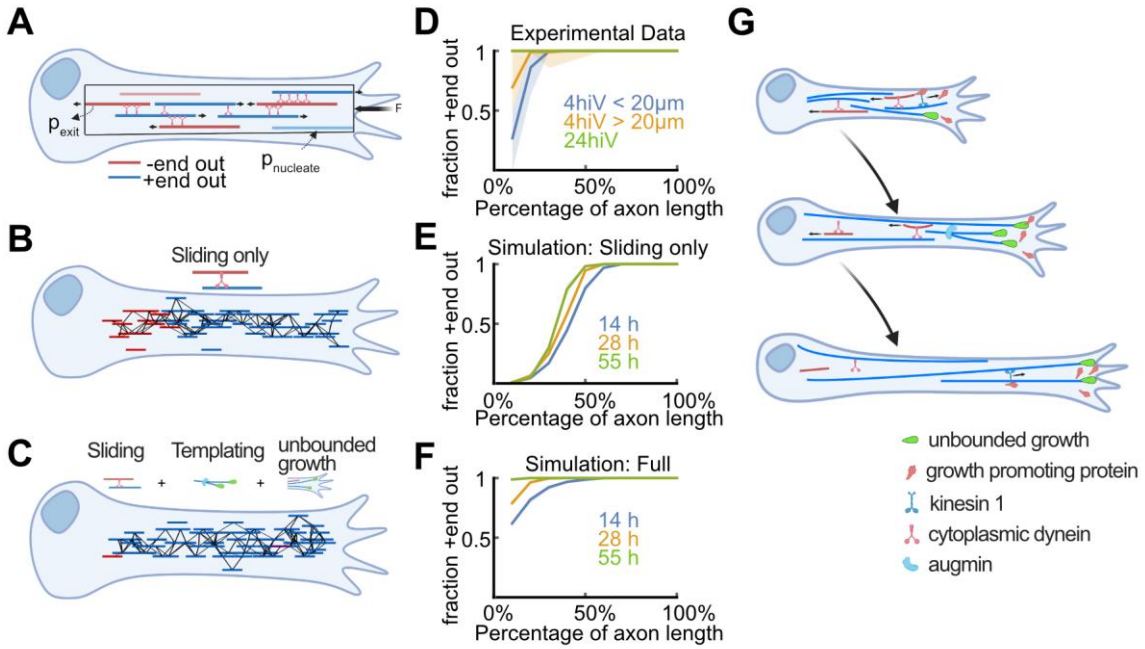

Figure 5: Biased stabilization of +end out MTs is required to establish uniform axonal MT orientation. (A) Schematic showing the MT sliding simulation and its relevant parameters. **(B-C)** Simulation results of MT dynamics. **(B)** Snapshot of a simulated axon with dynein-based sliding of MTs. -end out MTs accumulated within the proximal axon. **(C)** Snapshot of an axon simulated with sliding, augmin templating (new MTs were likely oriented into the same direction as their surrounding ones), and biased nucleation of +end out MTs at the tip. Much like in real axons, most MTs were oriented with their +end out throughout the axon. **(D)** Experimental profiles of MT orientation along the (normalized) axon length for axons that were cultured 4 hours in vitro (4hiV), separated into less than 20 µm or more than 20 µm long, and 24 hours in culture (24hiV). Lines represent bootstrapped medians and 95% confidence intervals. **(E-F)** Simulation profiles of MT orientation along the axon. **(E)** Profiles obtained from simulations with dynein-mediated sliding only at 3 different simulation timepoints. MT orientation was graded along the axon but, unlike in the experimental profiles shown in **(D)**, the proximal axon remained enriched with -end out MTs. **(F)** MT orientation profiles obtained from simulations with sliding, templating, and biased nucleation of +end out MTs at the axon tip. The observed gradual development of MT orientation along the axon is in excellent agreement with our experimental data **(D)**. **(G)** Summary of proposed mechanism for establishing MT orientation in axons. Red and blue lines represent -end out and +end out MTs, respectively. Green drop shapes indicate unbounded MT growth into the axon tip for +end out MTs. Kinesin 1 deposits MT growth promoting proteins, such as p150, at axon tips

858 (ERROR! REFERENCE SOURCE NOT FOUND.), leading to local unbounded growth of +end out MTs. Augmin templating and
859 cell body-directed sliding of -end out MTs further amplifies this bias. All three mechanisms together lead to a +end
860 out MT cytoskeleton.